Tracking 30-year evolution of subsidence in Shanghai utilizing multi-sensor InSAR and random forest modelling

Lu, Can; Xu, Hanqing; Yao, Qian; Liu, Qing; Bricker, Jeremy D.; Jonkman, Sebastiaan N.; Yin, Jie; Wang, Jun

DOI
10.1016/j.jag.2025.104606

Publication date
2025

Document Version
Final published version

Published in
International Journal of Applied Earth Observation and Geoinformation

Citation (APA)
Lu, C., Xu, H., Yao, Q., Liu, Q., Bricker, J. D., Jonkman, S. N., Yin, J., & Wang, J. (2025). Tracking 30-year evolution of subsidence in Shanghai utilizing multi-sensor InSAR and random forest modelling. *International Journal of Applied Earth Observation and Geoinformation*, *140*, Article 104606. https://doi.org/10.1016/j.jag.2025.104606

International Journal of Applied Earth Observation and Geoinformation 140 (2025) 104606

Contents lists available at ScienceDirect

International Journal of Applied Earth Observation and Geoinformation

journal homepage: www.elsevier.com/locate/jag

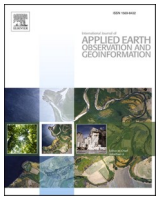

Tracking 30-year evolution of subsidence in Shanghai utilizing multi-sensor InSAR and random forest modelling

Can Lu [a,b,1], Hanqing Xu [a,b,c,1,*], Qian Yao [a,b], Qing Liu [a,b], Jeremy D. Bricker [d,e], Sebastiaan N. Jonkman [d], Jie Yin [a], Jun Wang [a,b,*]

[a] Key Laboratory of Geographic Information Science (Ministry of Education), School of Geographic Science, East China Normal University, Shanghai, China
[b] Institute for National Safety and Embergency Management, East China Normal University, Shanghai, China
[c] Institute of Eco-Chongming (IEC), East China Normal University, Shanghai, China
[d] Faculty of Civil Engineering and Geosciences, Delft University of Technology, Delft 2628CN, the Netherlands
[e] Department of Civil and Environmental Engineering, University of Michigan, Ann Arbor, MI 48109, United States

ARTICLE INFO

Keywords:
Land subsidence
Multi-sensor SAR
Time series fusion
Random Forest-SHAP

ABSTRACT

Land subsidence is a significant issue in many coastal megacities, including Shanghai, where it poses risks to infrastructure and economic stability. Although numerous studies have used SAR datasets to monitor land subsidence in Shanghai, multi-decadal displacement measurements obtained from multi-sensor SAR data remain unavailable. Moreover, the contributions and variations of driving factors behind the evolution of land subsidence remain poorly understood. This study employs multi-sensor SAR fusion method and a Random Forest model, along with Shapley Additive exPlanations (SHAP), to examine subsidence evolution and assess the influence of key drivers over the past 30 years. The results show that severe subsidence has spread from central urban areas to surrounding suburban regions, particularly in the eastern coastal and southern industrial zones in Shanghai. SHAP analysis identified that evapotranspiration, sediment thickness, and groundwater extraction were the dominant factors in the early stage of subsidence, while recent groundwater management and recharge practices have significantly mitigated the subsidence rate. These findings demonstrate the shifting importance of different subsidence factors over time and provide valuable insights for long-term prevention and control measures.

1. Introduction

Land subsidence leads to a decline in surface elevation, which affects infrastructure and increases flood risks in coastal regions. It is driven by both natural processes (e.g., sediment compaction) and human activities (e.g., fluid extraction) (Bagheri-Gavkosh et al., 2021; Nicholls et al., 2021; Shirzaei et al., 2021; Hasan et al., 2023; Huning et al., 2024). Over 200 locations across 34 countries report significant subsidence, with an estimated 12 million km^2 of land at risk globally (Shirzaei and Bürgmann, 2018; Herrera-García et al., 2021; Fang et al., 2022; Buzzanga et al., 2023; Jiang et al., 2023; Ohenhen et al., 2023, 2024; Ao et al., 2024; Oelsmann et al., 2024; Wang et al., 2024; Thiéblemont et al., 2024). In China, subsidence-related economic losses average around USD 1.5 billion annually, with Shanghai alone incurring over USD 3.37 billion in damage between 2001 and 2020 (Erkens et al., 2015). As a rapidly growing economic center, Shanghai has experienced severe subsidence since 1921 due to intensive groundwater extraction, which peaked in the 1960s to 1980s. Although groundwater recharge policies have reduced extraction impacts, spatially uneven subsidence persists, requiring further investigation into its long-term evolution and primary driving mechanisms (Yang et al., 2020).

Interferometric Synthetic Aperture Radar (InSAR) enables large-scale monitoring of land subsidence with millimeter-level precision (Ferretti et al, 2001). Persistent Scatterer Interferometry (PS-InSAR) and Small Baseline Subset (SBAS) have proven effective in mitigating the interference in low-coherence areas (Berardino et al., 2002). PS-InSAR, for instance, was used to analyze subsidence rates across 99 coastal cities worldwide from 2015 to 2020, highlighting the significant role of

* Corresponding authors at: Key Laboratory of Geographic Information Science (Ministry of Education), School of Geographic Science, East China Normal University, Shanghai, China.
E-mail addresses: hqxu@chm.ecnu.edu.cn (H. Xu), jwang@geo.ecnu.edu.cn (J. Wang).
[1] Can Lu and Hanqing Xu contributed equally.

https://doi.org/10.1016/j.jag.2025.104606
Received 15 January 2025; Received in revised form 5 May 2025; Accepted 15 May 2025
Available online 20 May 2025

human activities, particularly groundwater extraction in driving subsidence (Wu et al., 2022). SBAS, due to its robustness against temporal and spatial decorrelation, is particularly advantageous for monitoring large-scale subsidence and has been extensively utilized in studies assessing surface subsidence in Chinese cities (Ao et al., 2024). Several InSAR-based studies have analyzed subsidence in Shanghai, focusing on short-term variations and localized effects (Dong et al., 2014; Zhao et al., 2019; Wang et al., 2022). However, most studies utilize data from a single satellite, often overlooking the potential of integrating multi-source, long-term available satellite data that dates back to 1991 (Damoah-Afari et al., 2007; Dong et al., 2023). Integrating multi-sensor data over extended periods enables a deeper understanding of land subsidence, especially related to urban development and groundwater recovery.

Traditional analysis of subsidence drivers often uses point-based correlations, linking subsidence to groundwater levels or aquifer characteristics (Zhu et al., 2015; Chen et al., 2019). While studies have applied machine learning to quantify contributions of human and natural factors, few have focused on whether the driving factors change over long-term processes, and the black-box nature of these methods limits their interpretability (Zhou et al. 2019; Chen et al., 2021; Qiao et al., 2024). Explainable AI (XAI) methods can enhance the transparency and interpretability of models. Among these methods, SHapley Additive exPlanations (SHAP) are particularly effective in improving the understanding of internal mechanisms of model predictions, offering insights into the role of various driving factors to subsidence (Lundberg and Lee, 2017; Davydzenka et al., 2024; Loi et al., 2024; Yoo et al., 2024).

In this study, we construct the first 30-year record of displacement in Shanghai using multi-sensor SAR data from ERS-1/2, Envisat ASAR, and Sentinel-1A/B, linked via a logistic model to create a continuous record from 1992 to 2023. We apply a Random Forest-SHAP model to determine the impacts of the factors driving subsidence. Our analysis identifies shifts in the primary drivers over time, highlighting the role of groundwater management in reducing subsidence and providing a framework for mitigating subsidence in coastal megacities.

2. Study area

Shanghai, a major city in the Yangtze River Delta region of China, covers an area of 6,340.5 km^2 (Fig. 1). The region's ground elevation generally ranges from 2 to 6 m above local mean sea level. The average annual temperature is approximately 15 °C, with total annual precipitation reaching 1,262.1 mm. The region is primarily composed of Quaternary sediments consisting of alternating clay and sand layers (200–300 m). Shanghai's groundwater is categorized into phreatic and confined aquifers based on formation time, genetic type, and water chemistry (Li et al., 2021).

3. Dataset and processing methods

3.1. Dataset

The dataset includes three C-band SAR images, GNSS and leveling benchmark data (for validating InSAR results), and land subsidence driving factors (Table 1). Specifically, SAR data from ERS-1/2 (June 1992 to October 2004), Envisat ASAR (September 2003 to September 2010), and Sentinel-1A/B (May 2016 to August 2023) were utilized. GNSS data were collected from the IGS network (https://network.igs.org/), and six leveling point records from 2017 to 2020 were provided by Zhang et al. (2023).

Data related to key hydrological, geological, and anthropogenic factors influencing land subsidence were also collected (Fig. 2). Groundwater extraction and recharge data for Shanghai districts from

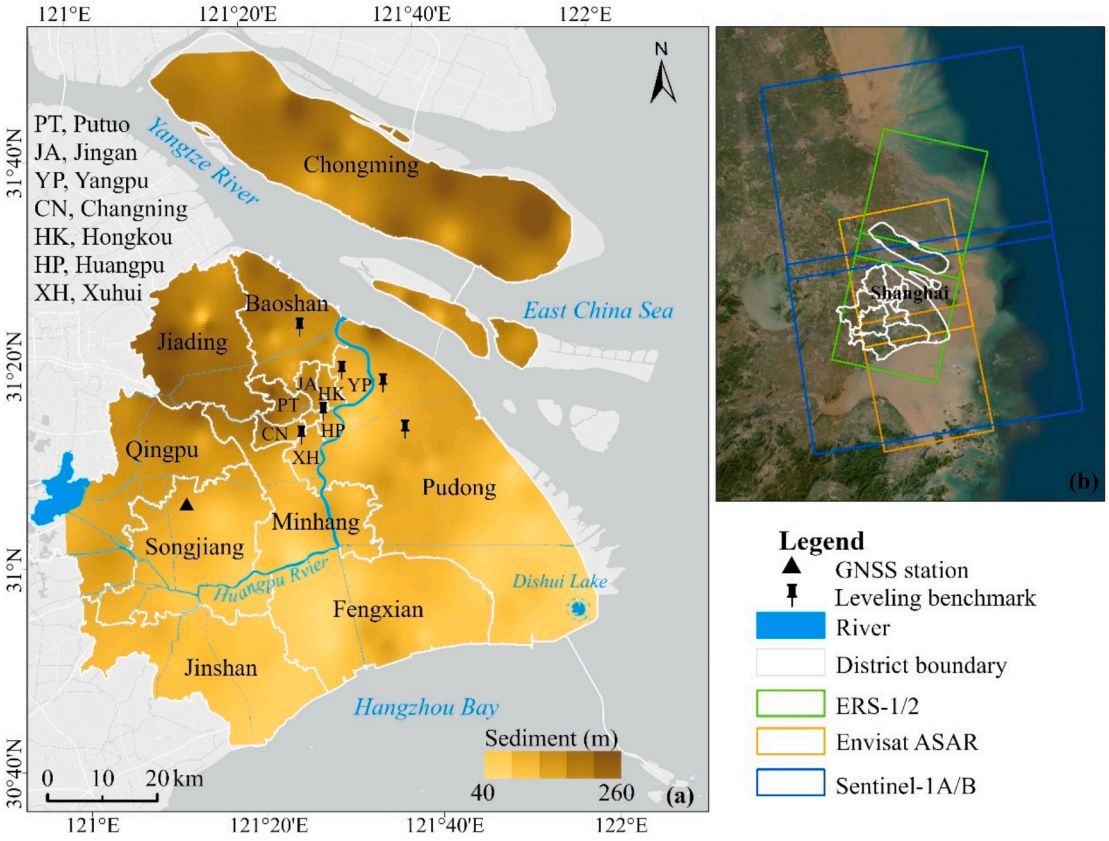

Fig. 1. Study site. (a) Location of Shanghai. The deep yellow areas represent the thickness of the deposited sediment layers. The major rivers are marked by blue lines. (b) Coverage areas of three C-band SAR datasets over the study region.

Table 1
Data used to monitor land subsidence and analyze its potential driving factors.

Data		Spatial resolution	Timespan	Additional information
SAR	ERS-1/2	30 m × 30 m	Jun 1992-Oct 2004	Flight Direction: Descending; Path: 3; No. of images: 86
	Envisat ASAR	30 m × 30 m	Sep 2003-Sep 2010	Flight Direction: Ascending; Path: 497; No. of images: 104
	Sentinel-1 A/B	5 m × 20 m	May 2016-Aug 2023	Flight Direction: Ascending; Path: 171; No. of images: 182
GNSS		Point	May 2016- Aug 2023	Vertical observations from the GPS station in Jinshan District, Shanghai.
Leveling data		Point	2017–2020	Observed from six leveling points, with their locations shown in Fig. 1.
Groundwater extraction		1 km	1990–2020	Groundwater extraction and recharge in confined aquifers.
Groundwater recharge		1 km	1990–2020	
Precipitation		1 km	2000–2020	Peng et al. (2019)
Evapotranspiration		1 km	2000–2020	Peng et al. (2017)
Building volume data		1 km	In 2000, 2005, 2010, 2015, 2020	Pesaresi and Politis (2022)
Population density		1 km	2000–2020	WorldPop
Deposited sediment		~ 1 km	–	Interpolated from borehole measurements.

1990 to 2020 were sourced from the Shanghai Geological Environment Bulletin (https://hd.ghzyj.sh.gov.cn/dzkc/dzhjbg). Precipitation and evapotranspiration data for the same period, with a 1 km spatial resolution, were provided by Peng et al. (2017, 2019). Building volume data for Shanghai from 2000 to 2020 were obtained from the Global Human Settlement dataset (https://human-settlement.emergency.copernicus.eu/datasets.php). A 1 km gridded population dataset, provided by WorldPop, was included to assess subsidence in populated areas (https://www.worldpop.org/). Additionally, deposited sediment thickness data (Fig. 1a) were included to represent geological factors influencing subsidence. Table 1 provides further details on the datasets. Multicollinearity tests were conducted to assess and reduce redundancy among the driving factors of land subsidence (supplementary Fig. S1) (Arabameri et al., 2020, Zhao et al., 2024).

3.2. Methods

3.2.1. SBAS technology

Prior to time-series inversion, all interferometric and geocoding steps were carried out in the commercial GAMMA software suite (version 201710) (Werner et al., 2000; Wegmüller et al., 2016). Single-look complex (SLC) products were imported, and master and slave SLCs were co-registered to ensure high-quality interferometric processing. Differential interferograms were subsequently generated and multi-looked, resulting in 149 pairs for ERS-1/2, 220 pairs for Envisat ASAR, and 413 pairs for Sentinel-1 (Fig. 3). The maximum spatiotemporal baselines of the three types of SAR data interferometry varied due to differences in sensors and data volume. The Digital Elevation Model (DEM) was used to simulate and remove the topographic phase, followed by geocoding of the interferogram (Farr et al., 2007).

Subsequently, the multi-look SBAS technique was applied to detect displacement using ERS-1/2, Envisat ASAR and Sentinel-1A/B data (Berardino et al., 2002). The time-series analysis was performed using the StaMPS software (version 4.1b) (Hooper, 2008). High coherence pixels (Hooper et al., 2007) were selected, and the phase difference of these pixels were converted into continuous phase changes through phase unwrapping, reflecting the true ground displacement (Costantini, 1998). Subsequently, atmospheric delay and orbital errors were corrected, and noise was removed. Finally, the processed phase of high coherence pixels was inverted to obtain the radar line-of-sight (LOS) displacement, then converted into vertical using the SAR image's incident angle, as shown in Eq. (1):

$$d_{vertical} = d_{LOS}/cos\theta \quad (1)$$

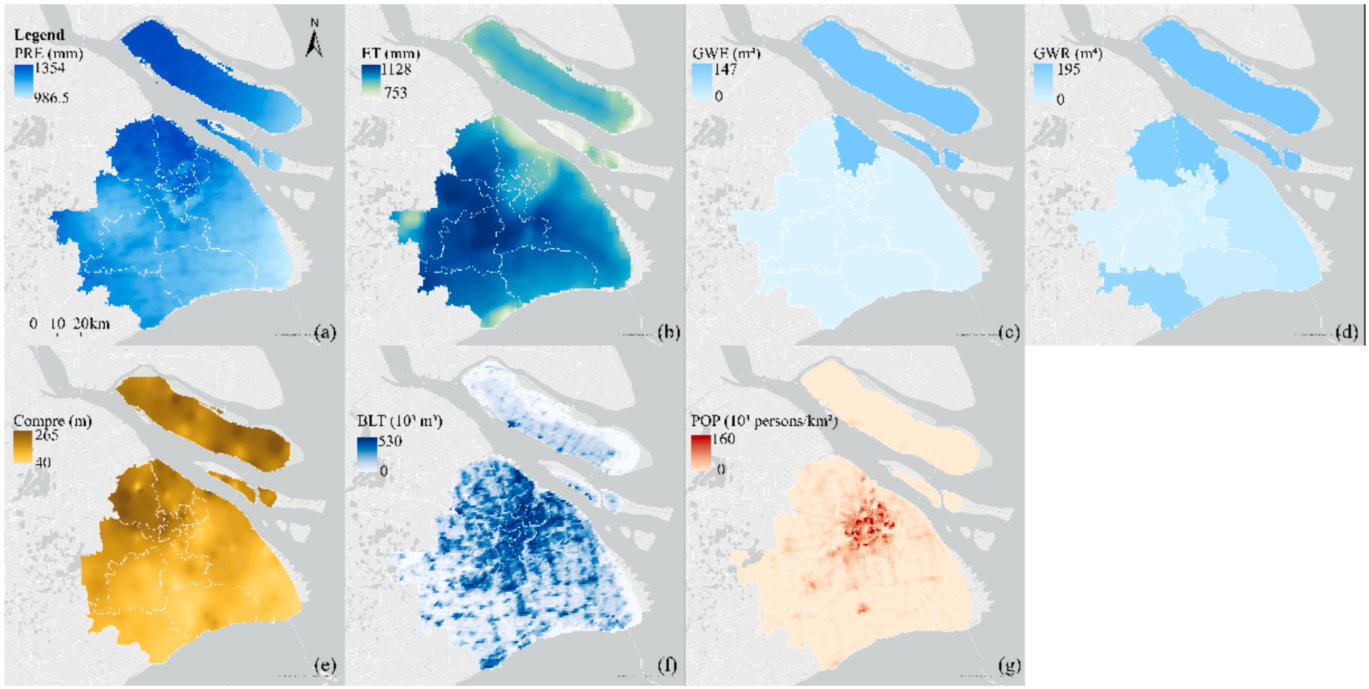

Fig. 2. Land subsidence drivers used for Random Forest-SHAP modeling: (a) precipitation, (b) evapotranspiration, (c) groundwater extraction, (d) groundwater recharge, (e) deposited sediment thickness, (f) building volume, and (g) population density. Some data spanning multiple years exist, but only the data from 2020 are currently being displayed.

Fig. 3. The baseline distributions in both spatial and temporal for the three SAR datasets.

where θ is the incident angle, and d_{LOS} denotes the displacement along the LOS direction. This conversion assumes negligible horizontal deformation, an assumption supported by previous studies indicating that vertical displacement is the dominant component of ground deformation in Shanghai (Wang et al., 2022). However, this simplification may not be applicable in all contexts. The 'strapdown' approach offers a promising alternative for capturing three-dimensional displacements in regions where horizontal movements are significant (Brouwer and Hanssen, 2024). This method addresses the underdetermined nature of 3D displacement estimation by incorporating minimal and largely undisputed contextual information about the deformation phenomenon, providing a practical solution to obtain physically meaningful estimates. Due to differences in SAR data sources, the parameters used in the processing vary accordingly. For detail of the parameters used in this analysis, please refer to supplementary Table S1.

3.2.2. Time series displacement fusion method

A comprehensive analysis of land subsidence changes requires long-term data, and therefore the displacement time series obtained from multi-sensor SAR images need to be effectively fused. There was variation in both the density and quantity of high coherence points generated by the three types of SAR data. A nearest-point matching method was then applied to roughly integrate the three datasets (Deng et al., 2017). First, using the coherence points from ERS-1/2 data as a reference, the closest points in space corresponding to the Envisat ASAR data were considered the same. Then, using the first date of ERS-1/2 as the reference, the date with the minimum subsidence error within the overlapping period was selected as the stitching time to link the data temporally. Since the time interval between Envisat ASAR and Sentinel-1 was relatively long, subsidence during this period was estimated using contour data from the Shanghai Geological Environment Bulletin. To assess potential interpolation errors, 100 points were randomly extracted across different subsidence levels along the original contour lines and compared with Kriging-derived values, obtaining a Root Mean Square Error (RMSE) of 3.2 and a Mean Absolute Error (MAE) of 1.5 to evaluate interpolation accuracy (supplementary Text S2, Table S2). Finally, the coherence points from ERS-1/2 and Envisat ASAR were matched with the Sentinel-1 results, and a logistic regression model was applied to integrate the multi-sensor InSAR time series. The model is as follows (Dong et al., 2023):

$$d(t) = \frac{D}{1 + e^{-k(t-t_0)}} + b \tag{2}$$

where $d(t)$ represents the modeled displacement at the coherence points, D denotes the potential maximum displacement, and k controls the gradient of the logistic regression curve, while time t_0 determines the inflection point of the curve.

The model parameters were determined by minimizing the objective function, which represents the squared difference between the actual and estimated displacement. Here, v_j^i represents the observed measurements at the j-th time of the i-th series, reflecting the actual land subsidence values. The parameter b^i acts as an offset for the i-th time series, accounting for baseline differences between individual time series. By minimizing the sum of squared errors, the parameters are optimized through a nonlinear least squares method, ensuring an accurate fit for the time series data (Wright, 2006). The objective function is given by:

$$\phi\left(D, k, t_0, b^i\right) = \sum_{i,j}\left(v_j^i - \left(\frac{D}{1 + e^{-k\left(t_j^i - t_0\right)}} + b^i\right)\right)^2 \quad i \in 1, 2, \cdots, N; j \in 1, 2, \cdots, M_i \tag{3}$$

The initial parameters are set to provide a reasonable starting point for the optimization process:

$$\begin{cases} b^{i,init} = 0, i \in 1, 2, \cdots, N \\ k^{init} = \dfrac{1}{t_{M_N}^N - t_1^1} \\ t_0^{init} = \dfrac{t_{M_N}^N + t_1^1}{2} \\ D^{init} = v_{0_{M_N}}^N - v_{0_1}^1 \end{cases} \tag{4}$$

where $b^{i,init}$ is initialized to 0, assuming no baseline offset at the outset. k^{init}, t_0^{init}, and D^{init} are determined based on the temporal and displacement ranges of the data, ensuring that the initial estimates align with the overall trends of the time series. This approach helps facilitate convergence during the optimization process.

3.2.3. Random Forest – SHAP model

Random Forest works by building multiple decision trees and aggregating their predictions, which improves the model's accuracy and robustness. This ensemble learning method effectively handles high-dimensional feature data. The algorithm splits the data into feature and target variables, building multiple trees using random subsets of samples and features. Each tree generates a prediction for the target variable, and the final output is an aggregation of these predictions. Furthermore, Random Forest provides feature importance scores by quantifying each feature's contribution across all decision trees.

To enhance the model's interpretability, SHAP is used to help explain and understand the decision-making process of the Random Forest model (Lundberg and Lee, 2017). The SHAP method computes the marginal impact of each feature on the prediction results, ensuring a fair and consistent distribution of contributions. This makes the model's explanations more transparent. The fundamental mathematical formulation of SHAP is as follows:

$$\phi_i(f) = \sum_{S \subseteq N \setminus \{i\}} \frac{|S|!(|N| - |S| - 1)!}{|N|!}[f(S \cup \{i\}) - f(S)] \tag{5}$$

where N denotes the complete set of features, and S is a subset of N that excludes a specific feature x_i, $f(S \cup \{i\})$ and $f(S)$ represent the prediction results using the features in S, with x_i included and excluded, respectively.

The subsidence at each coherence point is denoted as $y = [y_1, y_2, \cdots, y_i, \cdots, y_m]$ for $T_{1,2,\cdots,n}$, where m represents the number of the points and T represents the years. For each point, the values of the seven driving factors listed in Table 1, used for subsidence contribution analysis, are extracted to construct the vector $x = [x_1, x_2, \cdots, x_j, \cdots, x_7]$. These driving factors are then used as inputs to predict subsidence for 2000 and 2020, with the SHAP model used to interpret the predictions. The overall

methodology is summarized in Fig. 4.

4. Results

4.1. Spatial and temporal characteristics of displacement in Shanghai

Cross-comparisons of corresponding points within the overlapping regions were conducted to evaluate the displacement results of ERS-1/2 and Envisat ASAR. For the ERS-1/2 data, the sparse and dispersed coherence points resulted in a root mean square error (RMSE) of 3.64 mm/yr (Fig. 5a). In contrast, the Envisat ASAR data exhibited more concentrated coherence points, achieving a lower RMSE of 3.11 mm/yr (Fig. 5b). Validation against leveling and GPS vertical component data confirmed alignment with the average subsidence of coherence points within a 100-meter buffer zone, with leveling RMSE of 8.90 mm and GPS RMSE of 18.77 mm (Fig. 5c and 5d). For the comparison, only the vertical component of the GNSS data was used, with plate motions removed, and both GPS and InSAR results were transformed into the same coordinate system (WGS84) to ensure consistency. Additionally, subsidence contour data from the years 1996–2001 and 2002–2006, as published in the Shanghai Geological Bulletin, were collected for validation. The results demonstrated a generally consistent spatial pattern with the data obtained from ERS-1/2 and Envisat ASAR (Fig. S2). The validations demonstrate that all three datasets meet the accuracy requirements.

The spatial pattern of displacement across Shanghai based on different SAR data is shown in Fig. 6. Uplift is shown by positive values (blue), while negative values (red) indicate subsidence. ERS-1/2 data (1992–2004) identified 99,371 coherence points (Fig. 6a). During this period, severe subsidence was concentrated in central Shanghai, showing the maximum subsidence of 352 mm in central urban area, and extended into the southeastern Pudong. Envisat ASAR data (2003–2010) identified 1,521,981 coherence points (Fig. 6b), showing a reduction in central urban area subsidence, but intensified subsidence along the coastal regions of Pudong, where maximum cumulative subsidence reached 237 mm. Sentinel-1 data (2016–2023) obtained 994,705 coherence points, indicating further intensified subsidence in the eastern and southern coastal areas, with a peak total subsidence of 206 mm (Fig. 6c). The observed spatial trends in this study are consistent with previous monitoring results of land subsidence in Shanghai (Zhao et al.,2019; Wang et al., 2022).

4.2. Fusion of multi-sensor InSAR time series

To fuse the time series from three types of SAR images, the methodology described in Section 3.2.2 was applied. Using point P1 as a case (location shown in Fig. 8), the segmented time series were linked to construct a continuous long-term land subsidence time series. The fused time series shows a good alignment with the fitted curve (Fig. 7). Subsequently, the time series for all coherence points are integrated to construct the long-term land subsidence in Shanghai from 1992 to 2023. The logistic model effectively captured the observed pattern, with subsidence initially accelerating and gradually stabilizing.

The spatial distribution of cumulative land subsidence over 30 years revealed three distinct subsidence funnels situated within the central urban area, Pudong District, and the southern coastal region of Shanghai (Fig. 8). The maximum cumulative subsidence for these areas was 388 mm, 605 mm, and 363 mm, respectively. Taking P1 in the central urban area as an example, the temporal variation in the subsidence rate can be observed. In the initial phase, the subsidence rate was relatively fast, as evidenced by the steep slope of the fitting curve from 1992 to 2008 (Fig. 7). Over time, the subsidence rate gradually slowed, and the curve flattened, indicating that the subsidence process is progressively entering a stable state.

4.3. Relative importance of driving factors

Multicollinearity tests were performed to evaluate the correlations among the driving factors. The Variance Inflation Factor (VIF) values for all factors are below 3, demonstrating that the factors are suitable for incorporation into the model (Fig. S1). Based on the fused displacement time-series and associated driving factors data, we constructed a Random Forest-SHAP model to predict and interpret its driving factors. A total of 94,438 coherence points were randomly split, with 80%

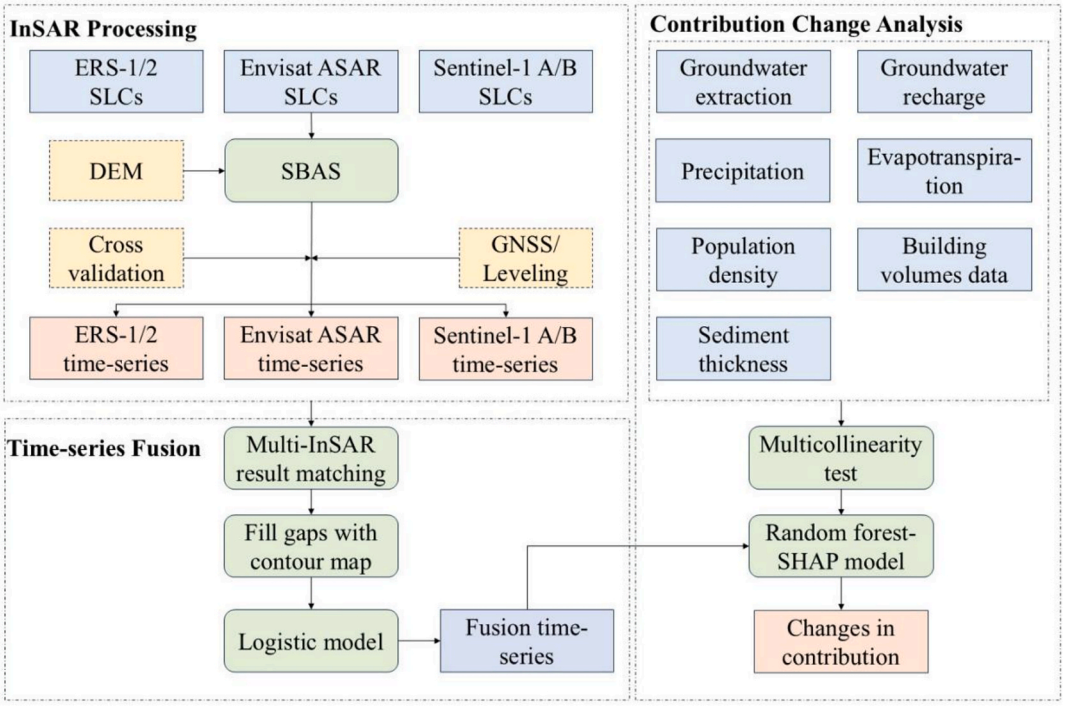

Fig. 4. Flowchart of methodology.

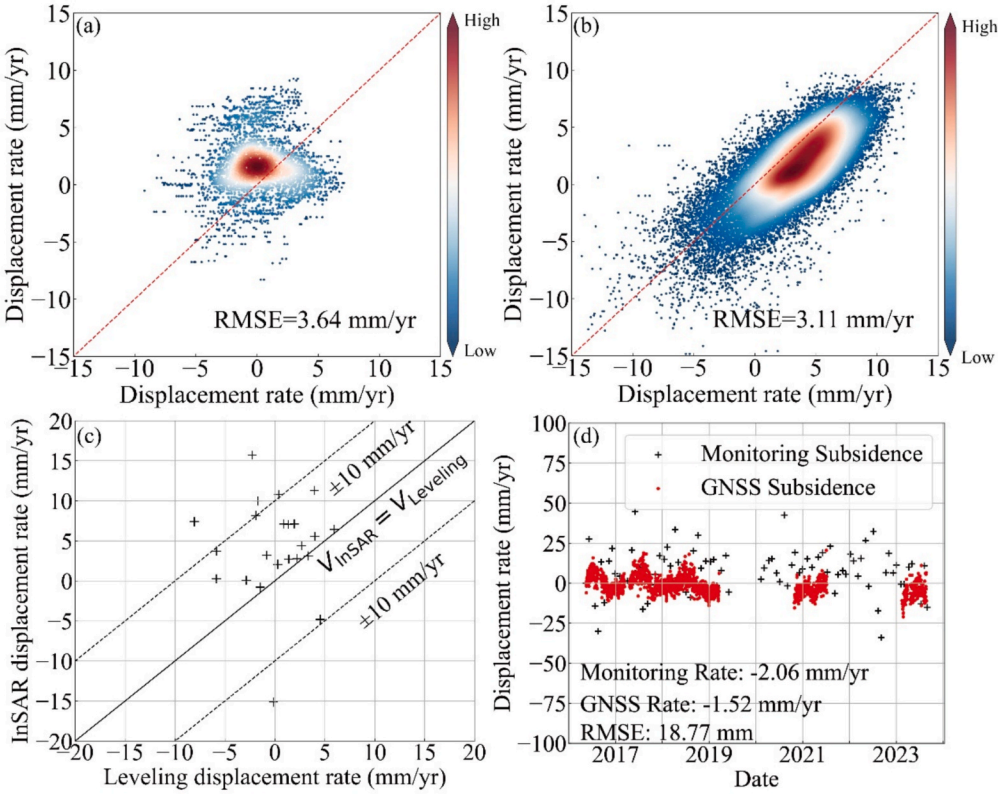

Fig. 5. Data Validation and multi-sensor InSAR displacement results. (a) Cross-validation results for the overlapping region of ERS-1/2 data. (b) Cross-validation results for the overlapping region of Envisat ASAR data. (c) Validation of InSAR-derived Sentinel-1 A/B velocities against leveling benchmark data. (d) Validation of InSAR-derived Sentinel-1 A/B velocities against GNSS-based velocities.

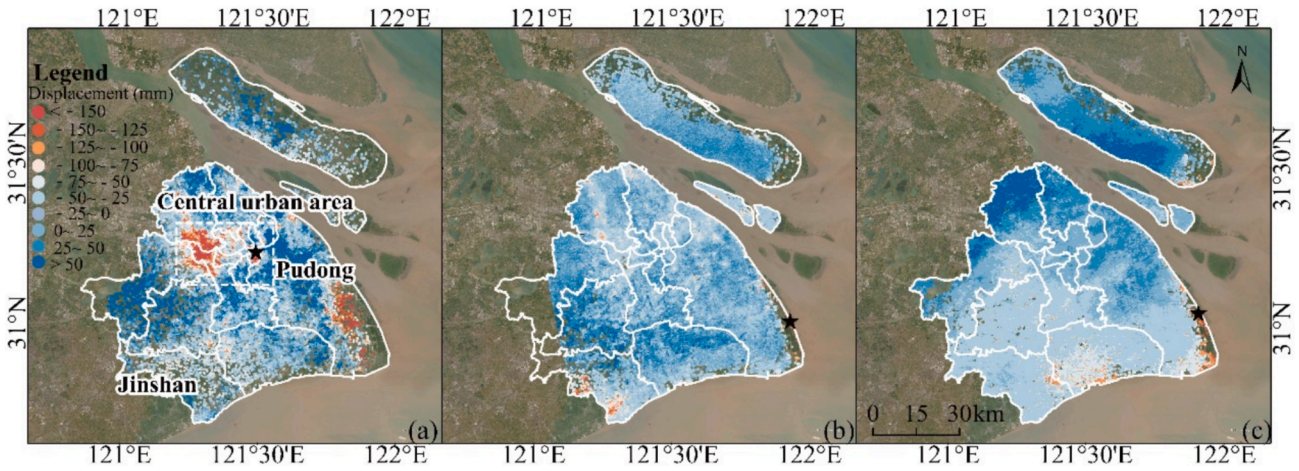

Fig. 6. Cumulative land subsidence across Shanghai. (a) ERS-1/2 (1992–2004). (b) Envisat ASAR (2003–2010). (c) Sentinel-1 A/B (2016–2023). The black pentagram represents the location with the maximum subsidence during the monitoring period.

allocated for training the model and 20% reserved for testing. To account for temporal variations and minimize the risk of overfitting, the model was trained separately on data from 2000 and 2020, ensuring that predictions for each year were independent. The model was trained with 'n_estimators' set to 300, achieving high accuracy for subsidence predictions in 2000 and 2020, with R^2 scores of 0.96 (Fig. 9).

Fig. 10 (a) and (b) show the contribution proportions of the driving factors, (c) and (d) display the SHAP decision plots, where each line represents a data point; 1,000 data points were selected for display in these plots. Fig. 10 (e) and (f) show the SHAP summary plots, where positive SHAP values indicate uplift, while the negative values represent subsidence. Red and blue correspond to high and low feature values, respectively, with their associated positive or negative contributions to the model's predictions. In 2000, evapotranspiration (ET) and deposited sediment thickness (Compre) were the primary contributors, accounting for 26% and 25% of subsidence, respectively. Precipitation (PRE) contributed 15% and groundwater extraction (GWE) accounted for 9%, with minimal impact from groundwater recharge (GWR). The decision plot shows that Compre and ET lines have a large divergence and have the most significant impact on the model (Fig. 10). SHAP analysis reveals a significant negative correlation between land subsidence and both Compre and ET, where higher values of these factors (indicated in

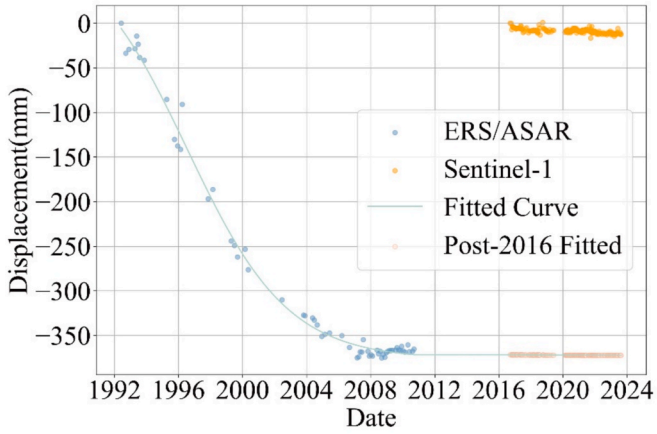

Fig. 7. Individual and fused multi-sensor InSAR time series with the model-fitting curve. The orange circles represent the original Sentinel-1 monitoring results, with the displacement of the first date set to zero, while the pink circles represent the logistic regression fitting results.

red on the SHAP plot) associated with greater subsidence. In contrast, PRE intensity shows a significant positive correlation with land subsidence.

By 2020, GWR became the primary driving factor, accounting for 27% of subsidence, followed by Compre at 18%. Contributions from ET and GWE decreased significantly, while the impacts of other factors remained relatively stable. The decision plot shows that the GWE line exhibits smaller divergence, while the GWR line shows an increased level of divergence. SHAP values indicated that GWR and PRE had a positive association with subsidence, suggesting that higher levels were linked to uplift. In contrast, Compre, along with ET and BLT, still demonstrated a significant negative impact on land subsidence. Although GWE still exhibited some negative influence, its SHAP range narrowed. Notably, while the contributions of BLT and POP remained stable, their SHAP ranges broadened.

The relative importance of various driving factors shifted from 2000 to 2020. The contribution of GWR increased by 21% compared to 2000, while that of GWE decreased by 8%, reducing its significance. The hydrological factors (GWE and GWR, ET, and PRE) made substantial combined contributions in both 2000 and 2020, accounting for 57% and 64% of subsidence, respectively. These factors influence land subsidence directly or indirectly by affecting groundwater levels. Compre consistently had a significant impact in both periods.

5. Discussion

5.1. SHAP-based interpretation of land subsidence drivers

From 2000 to 2020, the impact of groundwater extraction on land subsidence decreased significantly. This period saw a substantial reduction in groundwater extraction, with some areas halting extraction entirely and adopting recharge measures. Fig. 11 illustrates both the overall and district-level groundwater extraction and recharge in Shanghai from 1992 to 2020. The total groundwater extraction in Shanghai has shown a continuous decline over this period. It can be observed that in the central urban districts (Yangpu, Huangpu, Xuhui,

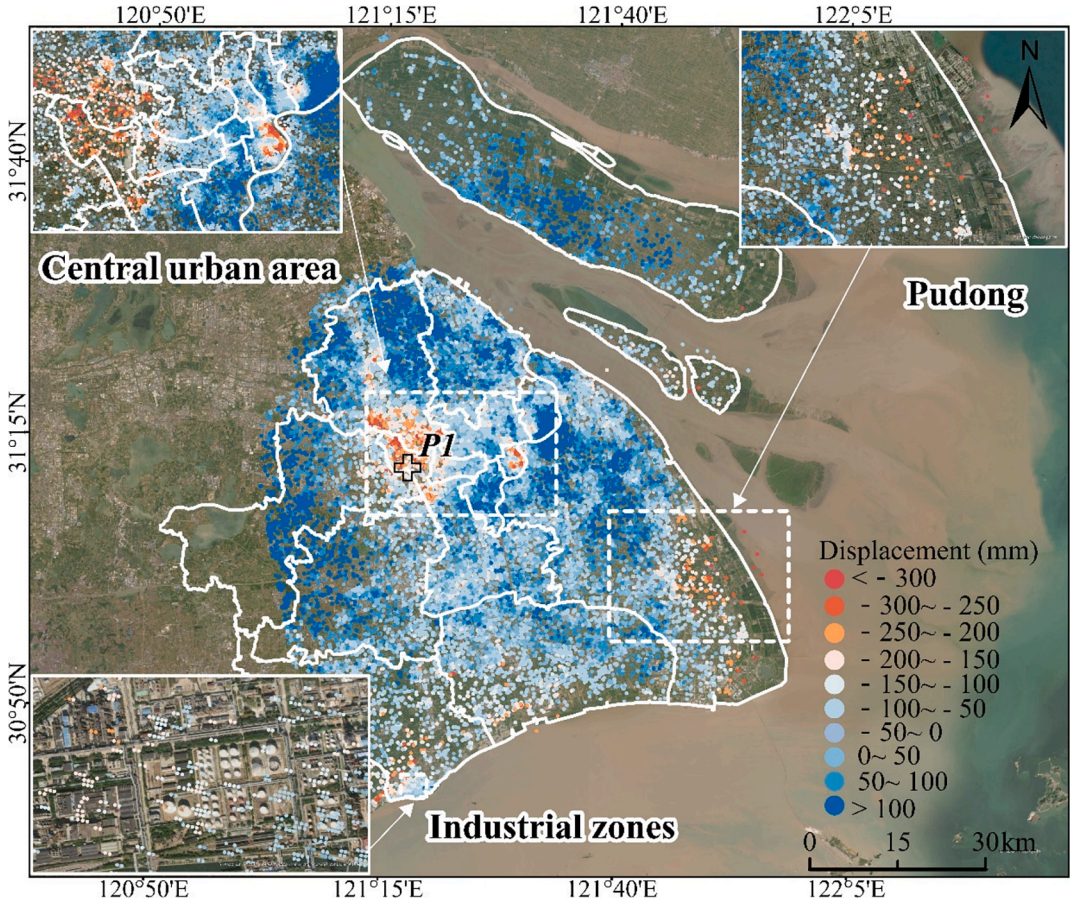

Fig. 8. Cumulative surface fusion displacement distribution from three SAR datasets. The white dashed box selects three subsidence centers within the study area for zooming in, situated within the central urban area, Pudong District, and the southern industrial zones, respectively. P1 is a subsidence point within the central urban area.

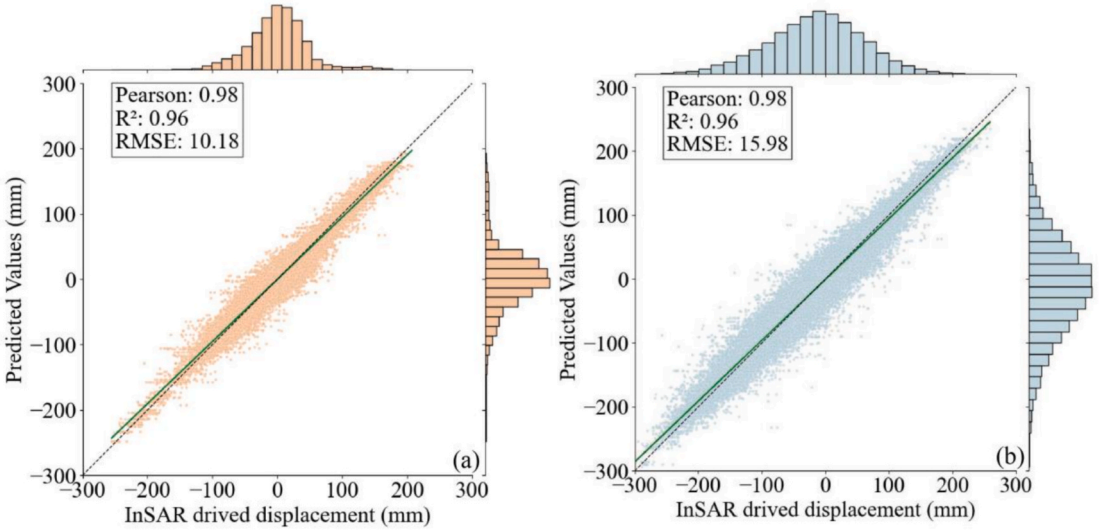

Fig. 9. Random Forest model prediction results. (a) 2000 and (b) 2020. Each data point represents the subsidence of a coherence point.

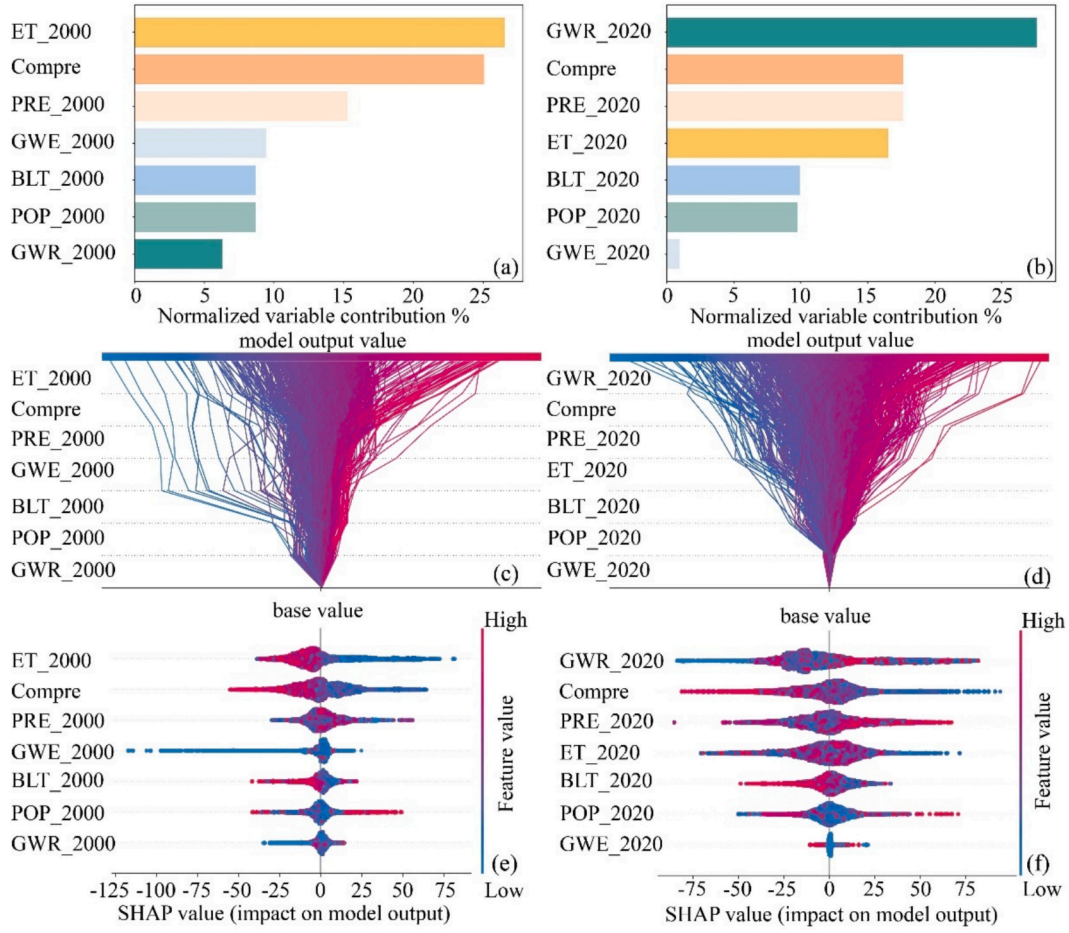

Fig. 10. Normalized impact and SHAP-based assessment of land subsidence driving factors. (a) Driving factors importance estimated with Random Forest in 2000. (b) Driving factors importance estimated with Random Forest in 2020. (c) SHAP decision plot of driving factors in 2000. (d) SHAP decision plot of driving factors in 2020. (e) SHAP summary plot of driving factors in 2000. (f) SHAP summary plot of driving factors in 2020. ET: evapotranspiration; Compre: deposited sediment thickness; PRE: precipitation; GWE: groundwater extraction; GWR: groundwater recharge; BLT: building volume data; POP: population density.

Putuo, Changning, Jingan, and Hongkou), groundwater recharge gradually exceeded extraction starting from 1992. In other districts, recharge began to surpass extraction around 2008. This shift reflects the effectiveness of groundwater management policies, including recharge initiatives and extraction limits, in mitigating subsidence. The SHAP values, clustered in the positive range, demonstrate the growing effectiveness of recharge in controlling subsidence by this time.

The thickness of the deposited sediment consistently influenced

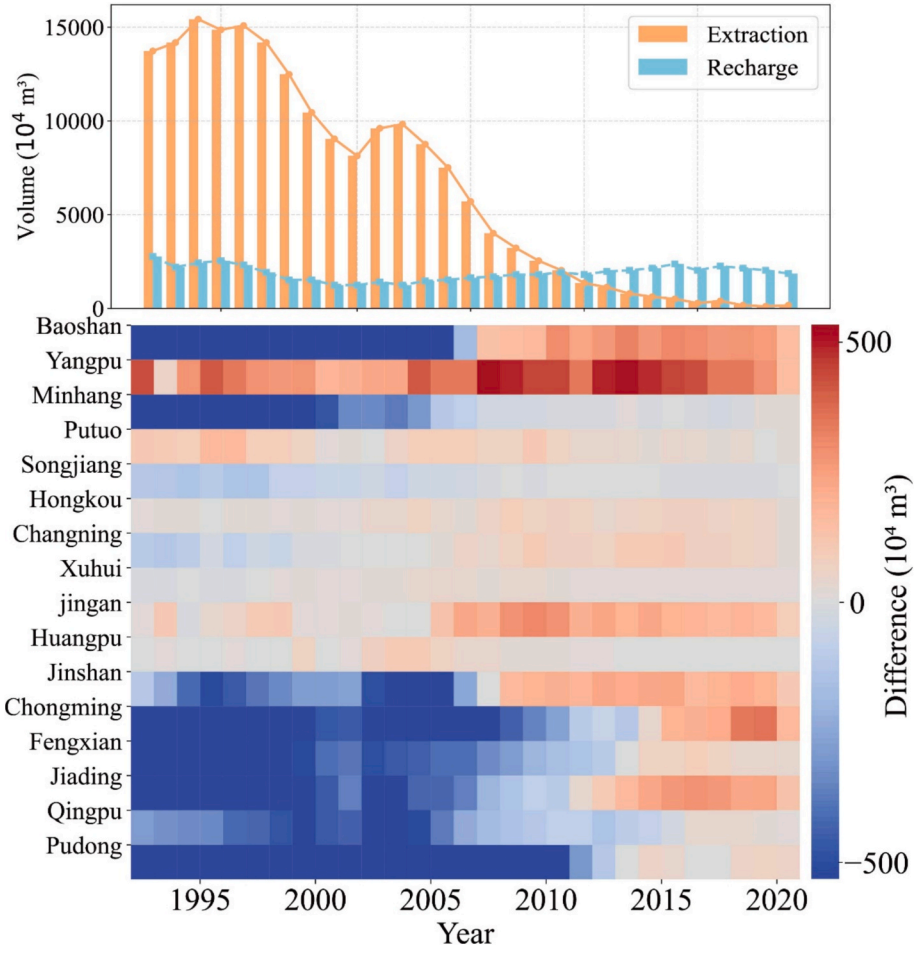

Fig. 11. Variations in groundwater extraction and recharge in Shanghai at both overall and district levels (1992–2020): Red indicates that recharge exceeds extraction, while blue indicates the opposite.

subsidence in both periods. The potential magnitude of subsidence is controlled by the thickness of the deposited sediment, with larger values typically indicating more pore space for compaction. Notably, areas with subsidence greater than 200 mm have thicker deposited sediment, as indicated by higher median thickness (Fig. 12a). This impact suggests that in regions with thicker deposited sediment, the likelihood of subsidence is higher. Therefore, geological conditions remain a crucial factor with a long-term and stable influence on this phenomenon.

Evapotranspiration and precipitation had relatively stable and indirect effects on subsidence across both periods, mainly through their influence on aquifer recharge (Fig. 12b). Increased precipitation can enhance groundwater recharge, while higher evapotranspiration may exacerbate groundwater depletion by limiting surface water infiltration. In 2020, the positive impact of precipitation became more evident, possibly due to higher precipitation levels or the implementation of rainwater utilization and 'sponge city' policies, which increased surface permeability and reduced runoff. However, increasing global irrigation demand, coupled with climate-induced changes in precipitation, evaporation, and surface water availability, is driving greater reliance on groundwater, exacerbating aquifer overextraction and land subsidence,

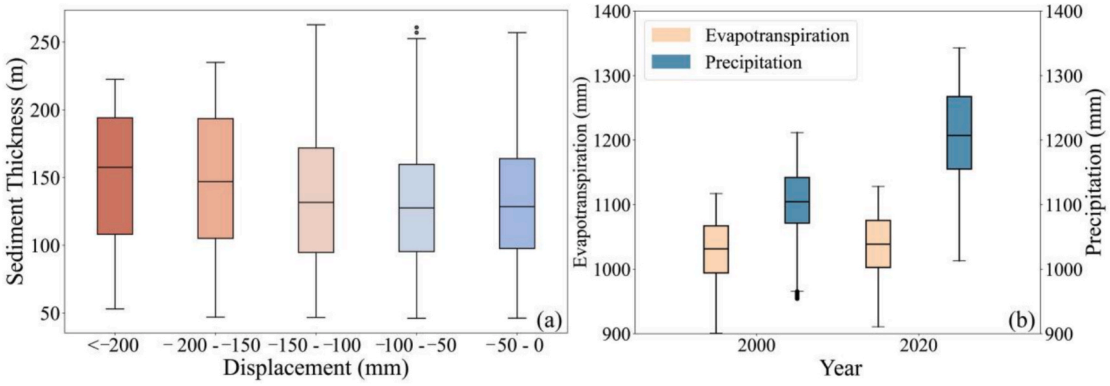

Fig. 12. Characteristics of land subsidence driving factors. (a) Deposited sediment thickness at different displacement levels. (b) Evapotranspiration and precipitation levels in 2000 and 2020.

while uncertainties in climate model projections further complicate future groundwater-related subsidence estimates (Huning et al., 2024). Projections from Coupled Model Intercomparison Project Phase 6 (CMIP6) indicate potential increases in extreme rainfall events and prolonged dry periods, which may lead to greater fluctuations in groundwater recharge and depletion (Copernicus Climate Change Service and Store, 2021). By 2040, a combination of factors, including human migration, urbanization, worsening droughts, declining groundwater levels, shifts in land cover and land use, sea level rise (SLR), and overall temperature increases, is projected to expand the global potential subsidence area by 7% and increase the population affected by subsidence by 30% (Herrera-García et al., 2021). Thus, future research should integrate hydrological modeling with climate projections to assess the long-term impacts of climate variability on subsidence risks, particularly in coastal megacities like Shanghai.

The contribution of building volume to subsidence showed an insignificant increase from 2000 to 2020. This modest impact is likely because urban areas had already experienced intensive development before 2000, reducing the relative effect of new construction (Xu et al., 2009, 2012). Subsidence tends to accelerate in recently developed areas (Ao et al., 2024), making new buildings in suburban and reclaimed areas vulnerable to subsidence due to sedimentary consolidation (Fig. 13). To further investigate the spatial relationship between construction activity and subsidence, we analyzed the proportion of major engineering projects relative to subsidence points across different districts (Fig. 14). The results indicate that districts with higher construction activity exhibit a greater proportion of subsidence points, whereas central urban areas, such as Huangpu, Xuhui, Changning, and Jingan, where construction intensity has declined, experience relatively lower subsidence rates. The SHAP results indicate that building volume is not a highly influential factor in subsidence. This may be because subsidence is also influenced by factors such as pile foundation depth and soil properties, which building volume alone does not capture (Ao et al., 2024). Additionally, the spatial density of input data influences the model's interpretation, with higher density in urban areas and lower density in suburbs. However, the impact of construction in suburban areas can be more significant due to rapid urbanization, potentially leading to an underestimation of its influence (Xu et al., 2016; Wang et al., 2022).

Population density showed no significant impact on subsidence in either period, likely due to its indirect role. Instead, higher population density may indirectly contribute to uplift by driving stricter groundwater management policies in response to increased water demand. Additionally, higher density often corresponds to infrastructure improvements, further supporting the indirect stabilization of subsidence.

5.2. Comparison with other subsiding megacities

The infrastructure of coastal cities could face severe impacts from flooding resulting from the combined effects of land subsidence and rising sea levels. Asian countries such as China, Indonesia, and Thailand are among the most heavily affected by these losses. In 11 coastal cities across Asia, land subsidence was primarily due to urban development and groundwater extraction, occurring at rates several times faster than the rise in sea levels (Takagi et al., 2023). Although some cities have seen a reduction in subsidence rates due to decreased groundwater extraction, subsidence continues to progress in places like Jakarta, Manila, and Bangkok.

Land subsidence in Jakarta was first observed in 1926 and has worsened over decades due to rapid population growth and industrial expansion. Since the 1980s, private groundwater extraction surged, with registered wells increasing from 352 in 1968 to 2,626 in 1998. After policy interventions, growth slowed, reaching 4,551 by 2016 (Batubara et al., 2023). However, GPS surveys (2015–2019) show northern coastal areas still sinking at 6.2 cm/yr, likely due to unregistered groundwater extraction (Abdullah et al., 2021).

In Bangkok, significant land subsidence began in the 1970s and peaked in the early 1980s at rates of up to 12 cm/yr (Phien-wej et al., 2006). In response, the government implemented groundwater regulation policies, successfully reducing subsidence (Babel et al., 2006). However, groundwater extraction rose from 1.2 million to over 2 million cubic meters per day between the early 1980s and 2000, causing subsidence to extend beyond the city center into suburban and provincial areas (Ahmed et al., 2024). Strict mitigation measures, including critical groundwater zones, and expanded surface water supply, have helped control urban subsidence, though peripheral regions remain vulnerable (Bremard, 2022).

In Manila, groundwater extraction has long been the primary driver of land subsidence. Tidal gauge records (1901–1965) showed a trend of

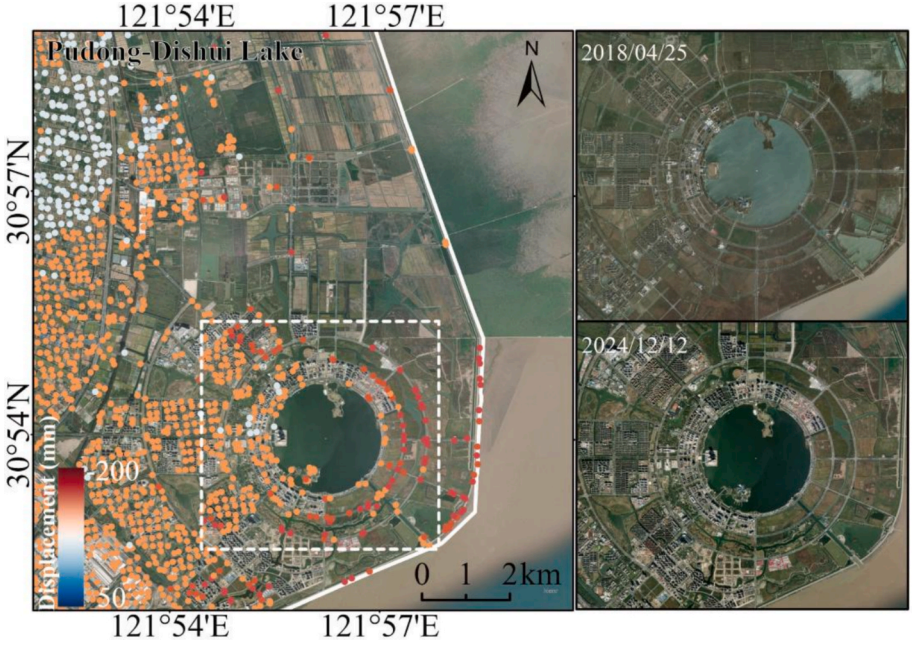

Fig. 13. Examples of land subsidence associated with construction. The white dashed box represents the Dishui Lake. The image in the top right is a remote sensing image from April 25, 2018, and the image in the bottom right is from December 12, 2024. During this period, Dishui Lake underwent construction.

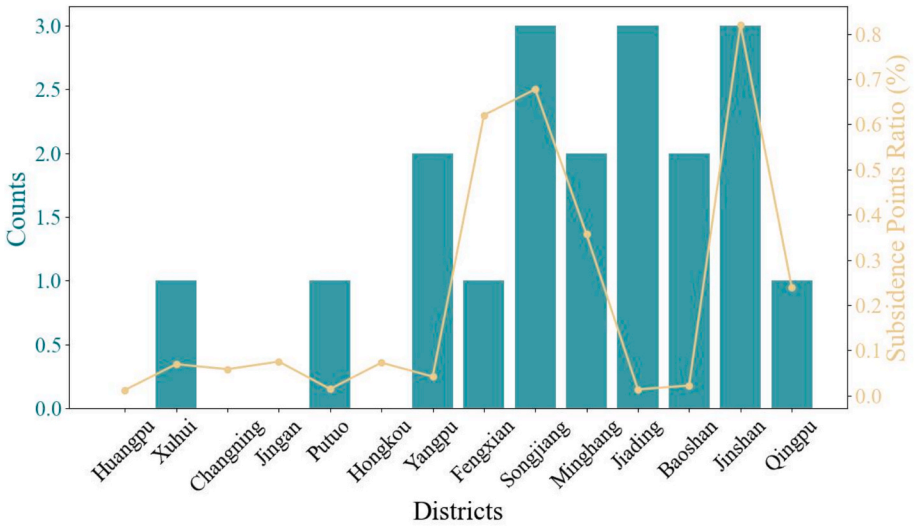

Fig. 14. The plot of the monitoring results of the Sentinel-1 dataset and related construction activities in each district.

1.5 mm/yr, later rising to 14.7 mm/yr, with earlier trends possibly linked to global sea-level rise (Siriwardane-de Zoysa et al., 2021). Since the 1970s, groundwater extraction has increased fivefold due to rapid population growth. Although the Water Code Amendment later banned deep wells within municipal boundaries, weak enforcement has allowed groundwater depletion to persist, worsening subsidence.

Shanghai has successfully implemented groundwater management policies that have reduced subsidence in certain areas, particularly in the central urban districts. Similar to Bangkok, Shanghai has experienced a shift in subsidence patterns due to urban expansion, indicating the need for comprehensive regional land-use planning. The experiences of these cities suggest that a combination of stricter groundwater policies, improved enforcement, and alternative water supply strategies could further enhance Shanghai's long-term subsidence mitigation efforts.

5.3. Integrated approaches to land subsidence prevention and mitigation

The findings of this study underscore the necessity of comprehensive policy interventions to mitigate land subsidence in rapidly urbanizing coastal megacities like Shanghai. Sustainable groundwater management remains critical, requiring the optimization of groundwater recharge and extraction through designated subsidence control zones with specific regulations. Additionally, enhanced rainwater collection and reuse strategies can reduce dependence on groundwater, mitigating long-term subsidence risks. Given the role of engineering activities in accelerating subsidence, stricter construction guidelines should be implemented, particularly in soft soil regions, alongside foundation design standards that account for long-term subsidence risks. Furthermore, policies should restrict high-density development in subsidence-prone areas to prevent excessive loading on soft soils. To support proactive risk management, remote sensing-based early warning systems should be developed, integrating InSAR monitoring and artificial intelligence-based prediction models to detect anomalies and issue timely warnings. Such a system would provide government agencies and stakeholders with critical information to implement targeted mitigation strategies.

6. Conclusions

This study provides a comprehensive analysis of land subsidence in Shanghai over the past 30 years using multi-sensor InSAR data, revealing a significant spatial shift in subsidence patterns from central urban districts to eastern coastal and southern industrial zones. The Random Forest-SHAP analysis highlights that while groundwater management policies have successfully mitigated excessive subsidence in certain areas, sediment thickness remains a persistent driver. These findings emphasize the need for sustainable urban planning strategies that account for evolving subsidence risks. Specifically, policymakers should integrate subsidence-prone zones into land-use planning, enforce stricter construction regulations in soft soil areas, and enhance groundwater recharge programs to maintain long-term stability.

Although this study provides long-term land subsidence data, the temporal resolution of the driving factor characteristics may be limited, affecting the ability to capture seasonal variations in subsidence. Future research should incorporate higher-resolution datasets (e.g., groundwater time series) and advanced machine learning techniques to improve prediction accuracy and further explore the interactions between climate change, human activities, and subsidence mechanisms.

CRediT authorship contribution statement

Can Lu: Writing – original draft, Visualization, Validation, Conceptualization. **Hanqing Xu:** Writing – review & editing, Supervision, Funding acquisition, Conceptualization. **Qian Yao:** Resources, Data curation. **Qing Liu:** Visualization, Validation. **Jeremy D. Bricker:** Writing – review & editing, Conceptualization. **Sebastiaan N. Jonkman:** Writing – review & editing, Conceptualization. **Jie Yin:** Writing – review & editing, Funding acquisition. **Jun Wang:** Writing – review & editing, Supervision, Funding acquisition.

Declaration of competing interest

The authors declare that they have no known competing financial interests or personal relationships that could have appeared to influence the work reported in this paper.

Acknowledgments

This research has been supported by the China National Key R&D Program (Grant No. 2023YFF0807000), the National Natural Science Foundation in China (Grant No. 42371088 and 42401087), the China Postdoctoral Science Foundation (Grant No. 2023 M731091), the Postdoctoral Fellowship Program of CPSF (Grant No. GZB20230217), the "Shu Guang" project supported by Shanghai Municipal Education Commission and Shanghai Education Development Foundation (Grant No. 21SG28), and the Shanghai Pilot Program for Basic Research (Grant No. TQ20240209).

Appendix A. Supplementary data

Supplementary data to this article can be found online at https://doi.org/10.1016/j.jag.2025.104606.

Data availability

Data will be made available on request.

References

Ao, Z., Hu, X., Tao, S., Hu, X., Wang, G., Li, M., Wang, F., Hu, L., Liang, X., Xiao, J., Yusup, A., Qi, W., Ran, Q., Fang, J., Chang, J., Zeng, Z., Fu, Y., Xue, B., Wang, P., Zhao, K., Li, L., Li, W., Li, Y., Jiang, M., Yang, Y., Shen, H., Zhao, X., Shi, Y., Wu, B., Yan, Z., Wang, M., Su, Y., Hu, T., Ma, Q., Bai, H., Wang, L., Yang, Z., Feng, Y., Zhang, D., Huang, E., Pan, J., Ye, H., Yang, C., Qin, Y., He, C., Guo, Y., Cheng, K., Ren, Y., Yang, H., Zheng, C., Zhu, J., Wang, S., Ji, C., Zhu, B., Liu, H., Tang, Z., Wang, Z., Zhao, S., Tang, Y., Xing, H., Guo, Q., Liu, Y., Fang, J., 2024. A national-scale assessment of land subsidence in China's major cities. Science 384 (6693), 301–306. https://doi.org/10.1126/science.adl4366.

Abdullah, F.M., Andriyanto, H., Nababan, J.R., Abdillah, F., Sulistyawan, R.I.H., 2021. Results of land subsidence measurement using GPS method in the Jakarta groundwater basin in 2015-2019. IOP Conf. Ser.: Earth Environ. Sci. 873, 11. https://doi.org/10.1088/1755-1315/873/1/012034.

Ahmed, S., Hiraga, Y., Kazama, S., 2024. Land subsidence in Bangkok vicinity: Causes and long-term trend analysis using InSAR and machine learning. Sci. Total Environ. 946, 174285. https://doi.org/10.1016/j.scitotenv.2024.174285.

Arabameri, A., Saha, S., Roy, J., Tiefenbacher, J.P., Cerda, A., Biggs, T., Pradhan, B., Ngo, P.T., Collins, A.L., 2020. A novel ensemble computational intelligence approach for the spatial prediction of land subsidence susceptibility. Sci. Total Environ. 726, 138595. https://doi.org/10.1016/j.scitotenv.2020.138595.

Babel, M. S., Gupta, A. D., Domingo, N. D. S., & Donna, N. (2006). Land subsidence: A consequence of groundwater over-exploitation in Bangkok, Thailand. International Review for Environmental Strategies, 6(2), 307-327. https://www.iges.or.jp/en/publication_do cuments/pub/peer/en/1203/IRES_Vol.6-2_307.pdf.

Bagheri-Gavkosh, M., Hosseini, S.M., Ataie-Ashtiani, B., Sohani, Y., Ebrahimian, H., Morovat, F., Ashraf, S., 2021. Land subsidence: A global challenge. Sci. Total Environ. 778, 146193. https://doi.org/10.1016/j.scitotenv.2021.146193.

Batubara, B., Kooy, M., Zwarteveen, M., 2023. Politicising land subsidence in Jakarta: How land subsidence is the outcome of uneven sociospatial and socionatural processes of capitalist urbanization. Geoforum 139, 1–9. https://doi.org/10.1016/j.geoforum.2023.103689.

Berardino, P., Fornaro, G., Lanari, R., Sansosti, E., 2002. A new algorithm for surface deformation monitoring based on small baseline differential SAR interferograms. IEEE Trans. Geosci. Remote Sens. 40 (11), 2375–2383. https://doi.org/10.1109/TGRS.2002.803792.

Bremard, T., 2022. Monitoring land subsidence: The challenges of producing knowledge and groundwater management indicators in the Bangkok metropolitan region. Thailand. Sustainability 14 (17), 10593. https://doi.org/10.3390/su141710593.

Brouwer, W.S., Hanssen, R.F., 2024. Estimating three-dimensional displacements with InSAR: The strapdown approach. J. Geod. 98 (12), 110. https://doi.org/10.1007/s00190-024-01918-2.

Buzzanga, B., Bekaert, D.P., Hamlington, B.D., Kopp, R.E., Govorcin, M., Miller, K.G., 2023. Localized uplift, widespread subsidence, and implications for sea level rise in the New York City metropolitan area. Sci. Adv. 9 (39), eadi8259. https://doi.org/10.1126/sciadv.adi8259.

Chen, B., Gong, H., Lei, K., Li, J., Zhou, C., Gao, M., Guan, H., Lv, W., 2019. Land subsidence lagging quantification in the main exploration aquifer layers in Beijing plain, China. Int. J. Appl. Earth Obs. Geoinf. 75, 54–67. https://doi.org/10.1016/j.jag.2018.09.003.

Chen, B., Gong, H., Chen, Y., Lei, K., Zhou, C., Si, Y., Li, X., Pan, Y., Gao, M., 2021. Investigating land subsidence and its causes along Beijing high-speed railway using multi-platform InSAR and a maximum entropy model. Int. J. Appl. Earth Obs. Geoinf. 96, 102284. https://doi.org/10.1016/j.jag.2020.102284.

Copernicus Climate Change Service, Climate Data Store, 2021. CMIP6 climate projections. Copernicus Climate Change Service (C3S) Climate Data Store (CDS). doi: 10.24381/cds.c866074c (Accessed on 01-March-2025).

Costantini, M., 1998. A novel phase unwrapping method based on network programming. IEEE Trans. Geosci. Remote Sens. 36 (3), 813–821. https://doi.org/10.1109/36.673674.

Damoah-Afari, P., Ding, X. L., Li, Z., Lu, Z., Omura, M., 2007. Six years of land subsidence in Shanghai revealed by JERS-1 SAR data. IGARSS 2007 IEEE International Geoscience and Remote Sensing Symposium. IEEE 2093–2097. doi: 10.1109/IGARSS.2007.4423246.

Davydzenka, T., Tahmasebi, P., Shokri, N., 2024. Unveiling the global extent of land subsidence: The sinking crisis. Geophys. Res. Lett. 51(4) e2023GL104497. https://doi.org/10.1029/2023GL104497.

Deng, Z., Ke, Y., Gong, H., Li, X., Li, Z., 2017. Land subsidence prediction in Beijing based on PS-InSAR technique and improved Grey-Markov model. Gisci. Remote Sens. 54 (6), 797–818. https://doi.org/10.1080/15481603.2017.1331511.

Dong, J., Guo, S., Wang, N., Zhang, L., Ge, D., Liao, M., Gong, J., 2023. Tri-decadal evolution of land subsidence in the Beijing Plain revealed by multi-epoch satellite InSAR observations. Remote Sens. Environ. 286, 113446. https://doi.org/10.1016/j.rse.2022.113446.

Dong, S., Samsonov, S., Yin, H., Ye, S., Cao, Y., 2014. Time-series analysis of subsidence associated with rapid urbanization in Shanghai, China measured with SBAS InSAR method. Environ. Earth Sci. 72, 677–691. https://doi.org/10.1007/s12665-013-2990-y.

Erkens, G., Bucx, T., Dam, R., Lange, G., Lambert, J., 2015. Sinking Coastal Cities. Proc. IAHS 372, 189–198. https://doi.org/10.5194/piahs-372-189-2015.

Fang, J., Nicholls, R.J., Brown, S., Lincke, D., Hinkel, J., Vafeidis, A.T., Du, S., Zhao, Q., Liu, M., Shi, P., 2022. Benefits of subsidence control for coastal flooding in China. Nat. Commun. 13 (1), 6946. https://doi.org/10.1038/s41467-022-34525-w.

Farr, T.G., Rosen, P.A., Caro, E., Crippen, R., Duren, R., Hensley, S., Kobrick, M., Paller, M., Rodriguez, E., Roth, L., Seal, D., Shaffer, S., Shimada, J., Umland, J., Werner, M., Oskin, M., Burbank, D., Alsdorf, D., 2007. The shuttle radar topography mission. Rev. Geophys. 45 (2). https://doi.org/10.1029/2005RG000183.

Ferretti, A., Prati, C., Rocca, F., 2001. Permanent scatterers in SAR interferometry. IEEE Trans. Geosci. Remote Sens. 39 (1), 8–20. https://doi.org/10.1109/36.898661.

Hasan, M.F., Smith, R., Vajedian, S., Pommerenke, R., Majumdar, S., 2023. Global land subsidence mapping reveals widespread loss of aquifer storage capacity. Nat. Commun. 14 (1), 6180. https://doi.org/10.1038/s41467-023-41933-z.

Herrera-García, G., Ezquerro, P., Tomás, R., Béjar-Pizarro, M., López-Vinielles, J., Rossi, M., Mateos, R.M., Carreón-Freyre, D., Lambert, J., Teatini, P., Cabral-Cano, E., Erkens, G., Galloway, D., Hung, W.C., Kakar, N., Sneed, M., Tosi, L., Wang, H., Ye, S., 2021. Mapping the global threat of land subsidence. Science 371 (6524), 34–36. https://doi.org/10.1126/science.abb8549.

Hooper, A., Segall, P., Zebker, H., 2007. Persistent scatterer interferometric synthetic aperture radar for crustal deformation analysis, with application to Volcán Alcedo. Galápagos. J. Geophys. Res. Solid Earth. 112 (B7). https://doi.org/10.1029/2006JB004763.

Hooper, A., 2008. A multi-temporal InSAR method incorporating both persistent scatterer and small baseline approaches. Geophys. Res. Lett. 35 (16). https://doi.org/10.1029/2008GL034654.

Huning, L.S., Love, C.A., Anjileli, H., Vahedifard, F., Zhao, Y., Chaffe, P.L., Cooper, K., Alborzi, A., Pleitez, E., Martinez, A., Ashraf, A., Mallakpour, I., Moftakhari, H., AghaKouchak, A., 2024. Global land subsidence: Impact of climate extremes and human activities. Rev. Geophys. 62 (4), e2023RG000817. https://doi.org/10.1029/2023RG000817.

Jiang, R., Lu, H., Yang, K., Chen, D., Zhou, J., Yamazaki, D., Pan, M., Li, W., Xu, N., Yang, Y., Guan, D., Tian, F., 2023. Substantial increase in future fluvial flood risk projected in China's major urban agglomerations. Commun. Earth Environ. 4 (1), 389. https://doi.org/10.1038/s43247-023-01049-0.

Li, M.G., Chen, J.J., Xu, Y.S., Tong, D.G., Cao, W.W., Shi, Y.J., 2021. Effects of groundwater exploitation and recharge on land subsidence and infrastructure settlement patterns in Shanghai. Eng. Geol. 282, 105995. https://doi.org/10.1016/j.enggeo.2021.105995.

Loi, C.L., Wu, C.C., Liang, Y.C., 2024. Prediction of tropical cyclogenesis based on machine learning methods and its SHAP interpretation. J. Adv. Model. Earth Syst. 16 (3), e2023MS003637. https://doi.org/10.1029/2023MS003637.

Lundberg, S. M., Lee, S. I., 2017. A unified approach to interpreting model predictions. NIPS 2017 In Proceedings of the 31st International Conference on Neural Information Processing Systems. NIPS 4765–4774. Curran Associates, Inc. Retrieved from https://papers.nips.cc/paper/7062-aunified-approach-to-interpreting-model-predictions.pdf.

Nicholls, R.J., Lincke, D., Hinkel, J., Brown, S., Vafeidis, A.T., Meyssignac, B., Hanson, S. E., Merkens, J.L., Fang, J., 2021. A global analysis of subsidence, relative sea-level change and coastal flood exposure. Nat. Clim. Change 11 (4), 338–342. https://doi.org/10.1038/s41558-021-00993-z.

Oelsmann, J., Marcos, M., Passaro, M., Sanchez, L., Dettmering, D., Dangendorf, S., Seitz, F., 2024. Regional variations in relative sea-level changes influenced by nonlinear vertical land motion. Nat. Geosci. 17 (2), 137–144. https://doi.org/10.1038/s41561-023-01357-2.

Ohenhen, L.O., Shirzaei, M., Ojha, C., Kirwan, M.L., 2023. Hidden vulnerability of US Atlantic coast to sea-level rise due to vertical land motion. Nat. Commun. 14 (1), 2038. https://doi.org/10.1038/s41467-023-37853-7.

Ohenhen, L.O., Shirzaei, M., Ojha, C., Sherpa, S.F., Nicholls, R.J., 2024. Disappearing cities on US coasts. Nature 627 (8002), 108–115. https://doi.org/10.1038/s41586-024-07038-3.

Peng, S., Ding, Y., Wen, Z., Chen, Y., Cao, Y., Ren, J., 2017. Spatiotemporal change and trend analysis of potential evapotranspiration over the Loess Plateau of China during 2011–2100. Agric. for. Meteorol. 233, 183–194. https://doi.org/10.1016/j.agrformet.2016.11.129.

Peng, S., Ding, Y., Liu, W., Li, Z., 2019. 1 km monthly temperature and precipitation dataset for China from 1901 to 2017. Earth Syst. Sci. Data 11 (4), 1931–1946. https://doi.org/10.5194/essd-11-1931-2019.

Pesaresi, M., Politis, P., 2022. GHS-BUILT-V R2022A-GHS built-up volume grids derived from joint assessment of Sentinel-2, Landsat, and global DEM data, for 1975-2030. Dataset, European Commission, Joint Research Centre, Brussels.

Phien-wej, N., Giao, P.H., Nutalaya, P., 2006. Land subsidence in bangkok. Thailand. Eng. Geol. 82 (4), 187–201. https://doi.org/10.1016/j.enggeo.2005.10.004.

Qiao, X., Chu, T., Krell, E., Tissot, P., Holland, S., Ahmed, M., Smilovsky, D., 2024. Interpretation and attribution of coastal land subsidence: An InSAR and machine learning perspective. IEEE J. Sel. Top. Appl. Earth Obs. Remote Sens. 17, 4768–4783. https://doi.org/10.1109/JSTARS.2024.3361391.

Shirzaei, M., Bürgmann, R., 2018. Global climate change and local land subsidence exacerbate inundation risk to the San Francisco Bay Area. Sci. Adv. 4 (3), eaap9234. https://doi.org/10.1126/sciadv.aap9234.

Shirzaei, M., Freymueller, J., Törnqvist, T.E., Galloway, D.L., Dura, T., Minderhoud, P.S., 2021. Measuring, modelling and projecting coastal land subsidence. Nat. Rev. Earth Environ. 2 (1), 40–58. https://doi.org/10.1038/s43017-020-00115-x.

Siriwardane-de Zoysa, R., Schöne, T., Herbeck, J., Illigner, J., Haghighi, M., Simarmata, H., Porio, E., Rovere, A., Hornidge, A.K., 2021. The 'wickedness' of governing land subsidence: Policy perspectives from urban Southeast Asia. PLoS ONE 16 (6), e0250208. https://doi.org/10.1371/journal.pone.0250208.

Zhao, F., Miao, F., Wu, Y., Xiong, Y., Gong, S., Sun, D., 2024. Land subsidence susceptibility mapping in urban settlements using time-series PS-InSAR and random forest model. Gondwana Res. 125, 406–424. https://doi.org/10.1016/j.gr.2023.09.019.

Takagi, H., Cao, A., Esteban, M., 2023. Cumulative Land Subsidence in Populated Asian Coastal Cities. J. Coast. River. Flood Risk 1. https://doi.org/10.59490/jcrfr.2023.0002.

Thiéblemont, R., Le Cozannet, G., Nicholls, R.J., Rohmer, J., Wöppelmann, G., Raucoules, D., Michele, M.D., Toimil, A., Lincke, D., 2024. Assessing current coastal subsidence at continental scale: Insights from Europe using the European Ground Motion Service. Earth's. Future 12 (8), e2024EF004523. https://doi.org/10.1029/2024EF004523.

Wang, K., Chen, J., Valseth, E., Wells, G., Bettadpur, S., Jones, C.E., Dawson, C., 2024. Subtle land subsidence elevates future storm surge risks along the Gulf Coast of the United States. J. Geophys. Res. Earth Surf. 129 (9), e2024JF007858. https://doi.org/10.1029/2024JF007858.

Wang, R., Yang, M., Yang, T., Lin, J., Liao, M., 2022. Decomposing and mapping different scales of land subsidence over Shanghai with X-and C-Band SAR data stacks. Int. J. Digit. Earth 15 (1), 478–502. https://doi.org/10.1080/17538947.2022.2036835.

Werner, C., Wegmüller, U., Strozzi, T., Wiesmann, A., 2000. Gamma SAR and interferometric processing software. Proc. ESA SP-461, ERS-Envisat Symp., Gothenburg, Sweden, 16–20 Oct. 2000, 1620. https://www.gamma-rs.ch/uploads/media/2000-1_GAMMA_Software.pdf.

Wegmüller, U., Werner, C., Strozzi, T., Wiesmann, A., Frey, O., Santoro, M., 2016. Sentinel-1 support in the GAMMA software. Proc. Comput. Sci. 100, 1305–1312. https://doi.org/10.1016/j.procs.2016.09.246.

Wright, S.J., 2006. Numerical optimization. Springer.

Wu, P.C., Wei, M., D'Hondt, S., 2022. Subsidence in coastal cities throughout the world observed by InSAR. Geophys. Res. Lett. 49 (7), e2022GL098477. https://doi.org/10.1029/2022GL098477.

Xu, Y., Shen, S., Du, Y., 2009. Geological and hydrogeological environment in Shanghai with geohazards to construction and maintenance of infrastructures. Eng. Geol. 109 (3–4), 241–254. https://doi.org/10.1016/j.enggeo.2009.08.009.

Xu, Y., Ma, L., Du, Y., Shen, S., 2012. Analysis of urbanisation-induced land subsidence in Shanghai. Nat. Hazards 63, 1255–1267. https://doi.org/10.1007/s11069-012-0220-7.

Xu, Y., Shen, S., Ren, D., Wu, H., 2016. Analysis of factors in land subsidence in Shanghai: A view based on a strategic environmental assessment. Sustainability 8 (6), 573. https://doi.org/10.3390/su8060573.

Yang, T., Yan, X., Huang, X., Wu, J., 2020. Integrated management of groundwater exploitation and recharge in Shanghai based on land subsidence control. Proc. IAHS 382, 831–836. https://doi.org/10.5194/piahs-382-831-2020.

Yoo, C., Xiao, H., Zhong, Q.W., Weng, Q., 2024. Unequal impacts of urban industrial land expansion on economic growth and carbon dioxide emissions. Commun. Earth Environ. 5 (1), 203. https://doi.org/10.1038/s43247-024-01375-x.

Zhang, J., Ke, C., Shen, X., Lin, J., Wang, R., 2023. Monitoring land subsidence along the subways in Shanghai on the basis of time-series InSAR. Remote Sens 15 (4), 908. https://doi.org/10.3390/rs15040908.

Zhao, Q., Ma, G., Wang, Q., Yang, T., Liu, M., Gao, W., Falabella, F., Mastro, P., Pepe, A., 2019. Generation of long-term InSAR ground displacement time-series through a novel multi-sensor data merging technique: The case study of the Shanghai coastal area. ISPRS J. Photogramm. Remote Sens. 154, 10–27. https://doi.org/10.1016/j.isprsjprs.2019.05.005.

Zhou, C., Gong, H., Chen, B., Li, X., Li, J., Wang, X., Gao, M., Si, Y., Guo, L., Shi, M., Duan, G., 2019. Quantifying the contribution of multiple factors to land subsidence in the Beijing Plain, China with machine learning technology. Geomorphology 335, 48–61. https://doi.org/10.1016/j.geomorph.2019.03.017.

Zhu, L., Gong, H., Li, X., Wang, R., Chen, B., Dai, Z., Teatini, P., 2015. Land subsidence due to groundwater withdrawal in the northern Beijing plain. China. Eng. Geol. 193, 243–255. https://doi.org/10.1016/j.enggeo.2015.04.020.